Acceleration of Range Points Migration-Based Microwave Imaging for Nondestructive Testing

Shuto Takahashi and Shouhei Kidera, *Member, IEEE*

***Abstract*—A microwave ultrawideband radar offers advantages of high-range resolution and deep penetration depth in low-loss media, and is a promising efficient nondestructive testing technique. The traditional delay-and-sum (DAS)-based imaging algorithm inherently suffers from insufficient accuracy in determining the detailed structure of any buried foreign body. As a promising alternative, the range points migration (RPM)-based imaging method has been developed. However, this method faces a problem in terms of high computational cost, particularly in the case of three-dimensional objects, because it requires a densely sampled outer boundary to maintain its reconstruction accuracy. Therefore, this study accelerates the RPM-based method without sacrificing the reconstruction accuracy, exploiting the feature of Envelope-based outer boundary extraction. Finite-difference time-domain numerical simulation and experimental results indicate that our proposed method accurately reconstructs small air cavities buried in a concrete object with considerably low computational cost.**

***Index Terms*—Microwave ultrawideband (UWB) radar, nondestructive testing, range points migration (RPM), three-dimensional (3-D) imaging.**

I. Introduction

THERE is a strong demand for microwave ultrawideband imaging for the high-speed, deep-penetrating nondestructive testing tools for crack detection in aging roads or tunnels with noncontact measurement. Various imaging approaches have been developed, and these can mainly be divided into two categories. One is based on the confocal approach [1] that uses the delay-and-sum (DAS) principle. The other is based on the inverse scattering scheme solving the domain integral equation and reconstructs the spatial distribution of complex permittivity using a tomographic observation model [2]. However, the confocal approach suffers from problems of high computational cost; moreover, there is inaccurate and low-resolution shape estimation for continuous boundaries, wherein the scattering center varies with the observation angle. Furthermore, the inverse scattering approach requires a large number of unknowns and an iterative procedure with computationally expensive forward solver.

To overcome the above difficulties, this study focuses on the range point migration (RPM)-based imaging method. The RPM converts a group of observed time delays to corresponding scattering centers using the Gaussian kernel estimator [3], which assesses the accumulation degree of the intersection points of candidate curves [4], [5]. The RPM algorithm uses a prior estimation of the outer boundary by the Envelope method [6], and a propagation path is obtained using each discretized outer boundary points that are calculated according to Snell's law. Thus, the computational cost and reconstruction accuracy significantly depend on the discrete interval of the outer boundary; therefore, in the case of a three-dimensional (3-D) object, huge computational costs are incurred.

In this study, we investigate a new RPM-based method to address the above issues, which we have recently proposed [7], by focusing on an important characteristic of the Envelope method: It can provide a continuous (not discretized) outer boundary, and an orbit of propagation path (named as candidate curve) can then be continuously derived. Using this property, this method calculates the intersection point of the candidate curves by minimizing a cost function, i.e., a discretization process is not required any more. This study demonstrates the effectiveness of the proposed method by the finite-difference time-domain (FDTD)-based numerical simulation and experimental tests considering a concrete object having a spiral air tube or multiple air cavities, and reveals that the proposed method reconstructs the internal target boundary more accurately, compared with the DAS-based traditional method, and remarkably reduces the computational cost compared with the original RPM-based imaging, without sacrificing the reconstruction accuracy.

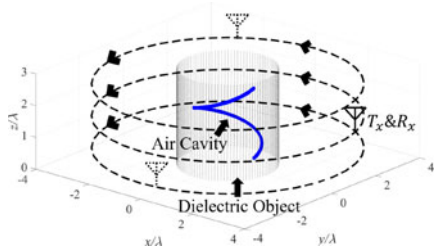

Fig. 1. Observation model.

II. Observation Model

Fig. 1 shows the observation model. It assumes that a homogeneous and low-loss medium (e.g. concrete) includes foreign bodies (e.g. air cavities or stainless-steel pipes). A set of transmitting and receiving antennas is scanned along the surface of the dielectric object. $s(\boldsymbol{L}, R)$ is defined as the signal after applying a matched filter to the recorded electric field, where $\boldsymbol{L} = (X, Y, Z)$ denotes the transmitting and receiving antennas locations, $R = ct/2$ is expressed by time t, and c is the speed of light in air. Range points extracted from the

Manuscript received February 2, 2018; accepted March 2, 2018. Date of publication March 7, 2018; date of current version April 5, 2018. This work was supported in part by JST, PRESTO, under Grant JPMJPR1771. *(Corresponding author: Shouhei Kidera.)*

S. Takahashi is with the Graduate School of Informatics and Engineering, The University of Electro-Communications, Tokyo 182-8585, Japan (e-mail: takahashi.shuto@ems.cei.uec.ac.jp).

S. Kidera is with the Graduate School of Informatics and Engineering, The University of Electro-Communications, Tokyo 182-8585, Japan, and also with Japan Science and Technology Agency, Saitama 332-0012, Japan (e-mail: kidera@uec.ac.jp).

Digital Object Identifier 10.1109/LAWP.2018.2812862

1536-1225 © 2018 IEEE. Personal use is permitted, but republication/redistribution requires IEEE permission.
See http://www.ieee.org/publications_standards/publications/rights/index.html for more information.

local maxima of $s(\boldsymbol{L}, R)$ are divided into two groups. One group is defined as $\boldsymbol{q}_{1,i} \equiv (\boldsymbol{L}_{1,i}, R_{1,i})$, where each point shows maximum $s(\boldsymbol{L}, R)$ at R. The remaining range points are categorized into $\boldsymbol{q}_{2,j} \equiv (\boldsymbol{L}_{2,j}, R_{2,j})$.

III. DAS-Based Method

Accuracy with DAS-based imaging is achieved by determining the propagation path in the dielectric medium using an accurate outer boundary model. However, the DAS-based method does not give accurate results for continuous-shaped boundary extraction. This is because the DAS algorithm assumes the scattering point to be invariant with respect to the observation point, which is valid for point-shaped target. On the contrary, in the case of continuous-shaped boundary, the dominant scattering center moves along its boundary, and the above assumption or principle of DAS method is invalid and incurs inaccuracy for shape estimation. Furthermore, the complex-value-based DAS method requires very small sampling intervals (within half of the wavelength of the dielectric medium) between the observation points to avoid the grating lobe effect, which is severe in media with high dielectric constants.

IV. RPM-Based Method

The RPM-based internal imaging method has been developed as a solution for the above problems; it achieves accurate boundary extraction by considering the variance in the scattering center. This method requires calculation of the intersection point as $\boldsymbol{p}^{\mathrm{int}}_{i,j,k}$ among three orbits of propagation paths, determined by $\boldsymbol{q}_{2,i}$, $\boldsymbol{q}_{2,j}$, and $\boldsymbol{q}_{2,k}$ [4], [5], named as candidate curves, for all possible combinations of range points $\boldsymbol{q}_2$. Specifically, the original RPM algorithm determines an optimal scattering center $\hat{\boldsymbol{p}}$ for $\boldsymbol{q}_{2,i}$ as

$$\hat{\boldsymbol{p}}(\boldsymbol{q}_{2,i}) = \underset{\boldsymbol{p}^{\mathrm{int}}_{i,l,m}}{\arg\max} \sum_{j,k} g(\boldsymbol{q}_{2,i}; \boldsymbol{q}_{2,j}, \boldsymbol{q}_{2,k}) \mathrm{e}^{\left\{ -\frac{\| \boldsymbol{p}^{\mathrm{int}}_{i,j,k} - \boldsymbol{p}^{\mathrm{int}}_{i,l,m} \|^2}{\sigma_r^2} \right\}} \tag{1}$$

where $g(\boldsymbol{q}_{2,i}; \boldsymbol{q}_{2,j}, \boldsymbol{q}_{2,k})$ is expressed as follows:

$$\begin{aligned} g(\boldsymbol{q}_{2,i}; \boldsymbol{q}_{2,j}, \boldsymbol{q}_{2,k}) \equiv\ & |s(\boldsymbol{q}_{2,j})| \mathrm{e}^{\left\{ -\frac{D^2_{XY,i,j}}{2\sigma^2_{XY}} - \frac{D^2_{Z,i,j}}{2\sigma^2_{Z}} - \frac{D^2_{R,i,j}}{2\sigma^2_{R}} \right\}} \\ & + |s(\boldsymbol{q}_{2,k})| \mathrm{e}^{\left\{ -\frac{D^2_{XY,i,k}}{2\sigma^2_{XY}} - \frac{D^2_{Z,i,k}}{2\sigma^2_{Z}} - \frac{D^2_{R,i,k}}{2\sigma^2_{R}} \right\}} \end{aligned} \tag{2}$$

where $D_{XY,i,j} = \sqrt{(X_2, i - X_2, j)^2 + (Y_2, i - Y_2, j)}$, $D_{Z,i,j} = |Z_2, i - Z_2, j|$, and $D_{R,i,j} = |R_2, i - R_2, j|$. σ_r, σ_{XY}, σ_Z, and σ_R are constants, which can be determined by considering the assumed sampling interval of observation point, detailed in [3]. Note that each candidate curve is expressed as a discrete form, each of which corresponds to an incident point on the outer boundary obtained by the Envelope method using $\boldsymbol{q}_1$. Fig. 2(a) shows the conceptual figure of a 2-D model, obtained using the original RPM-based method, where the intersection points of candidate curves are discretely determined. Thus, for a 3-D model, an extremely large number of discretized points must be processed for accurately calculating the intersection points.

A. Acceleration Algorithm

As a solution for the above problem, this study introduces an acceleration for the RPM-based method by avoiding discretization process for outer boundary and candidate curve extraction, which has been briefly introduced in [7]. Here, we focus on the notable feature of the Envelope method: It can express an outer dielectric boundary in an analytical (continuous) form by extracting the outer envelope of spheres, each of which has center $\boldsymbol{L}_{1,i}$ and radius $R_{1,i}$. Fig. 2(b) shows the intersection points of candidate curves in a continuous form. Then, the candidate curve for each $\boldsymbol{q}_{2,i}$ is also continuously derived because each point on candidate curve is uniquely determined by outer boundary point (continuously derived), using the Snell's law and the assumed dielectric constant. Then, the intersection point $\boldsymbol{p}^{\mathrm{int}}_{i,j,k}$ of the three candidate curves derived from $\boldsymbol{q}_{2,i}, \boldsymbol{q}_{2,j}, \boldsymbol{q}_{2,k}$ is calculated by minimizing the following cost function:

$$\begin{aligned} (\hat{\boldsymbol{r}}^{\mathrm{in}}_i, \hat{\boldsymbol{r}}^{\mathrm{in}}_j, \hat{\boldsymbol{r}}^{\mathrm{in}}_k) = \underset{\boldsymbol{r}^{\mathrm{in}}_i, \boldsymbol{r}^{\mathrm{in}}_j, \boldsymbol{r}^{\mathrm{in}}_k}{\arg\min} & \left\{ \| \boldsymbol{r}^{\mathrm{in}}_i - \boldsymbol{r}^{\mathrm{in}}_j \|^2 + \| \boldsymbol{r}^{\mathrm{in}}_i - \boldsymbol{r}^{\mathrm{in}}_k \|^2 \right. \\ & \left. + \| \boldsymbol{r}^{\mathrm{in}}_j - \boldsymbol{r}^{\mathrm{in}}_k \|^2 \right\} \end{aligned} \tag{3}$$

where $\| * \|$ is the Euclidean norm and $\boldsymbol{r}^{\mathrm{in}}_i$ denotes a point on the candidate curve corresponding to $\boldsymbol{q}_{2,i}$. The intersection point $\boldsymbol{p}^{\mathrm{int}}_{i,j,k}$ is represented as $\hat{\boldsymbol{r}}^{\mathrm{in}}_i$. Equation (3) is determined by the continuous variables $\boldsymbol{r}^{\mathrm{in}}_i$, $\boldsymbol{r}^{\mathrm{in}}_j$, and $\boldsymbol{r}^{\mathrm{in}}_k$, derived from the Envelope method. Note that the proposed method directly calculates the intersection point without generating the candidate curve, while the original one requires the preprocess for generating candidate curves, which is very time-consuming to maintain the accuracy. After calculating $\boldsymbol{p}^{\mathrm{int}}_{i,j,k}$ for all possible combinations of $\boldsymbol{q}_{2,i}, \boldsymbol{q}_{2,j}$, and $\boldsymbol{q}_{2,k}$, each scattering center is obtained by (1). Note that the computational complexity of each algorithm is $O(M^2N^2)$ for the original RPM-based algorithm and $O(MN^3)$ for the proposed algorithm, where M and N denote the sampling numbers of outer boundary and the number of the range points, respectively, and $O(*)$ is the Landau notation. In general, $M \gg N$ holds, thus the complexity of the proposed method is considerably reduced.

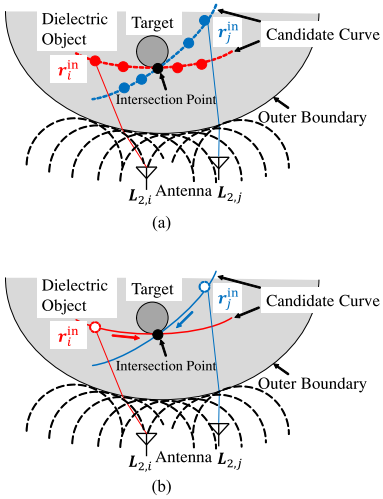

Fig. 2. Relationship of outer boundary, candidate curves, and their intersection point. (a) Original. (b) Proposed.

V. Performance Evaluation

A. FDTD-Based Numerical Test

A 3-D numerical simulation is performed using the FDTD forward solver to assess the performance of each method. The

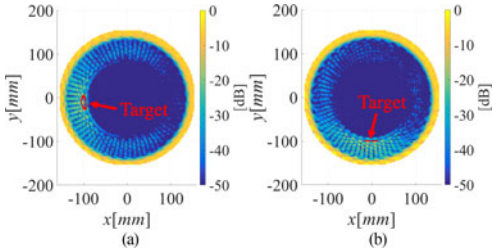

Fig. 3. Cross-sectional images obtained by the DAS-based method. (a) $z = 150$ mm. (b) $z = 200$ mm.

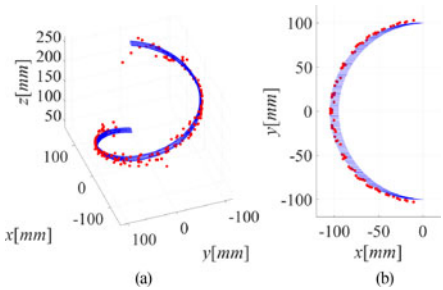

Fig. 4. Reconstructed points (red circle) by the original RPM. (a) 3-D view. (b) Sliced view (100 mm $\leq z \leq$ 200 mm).

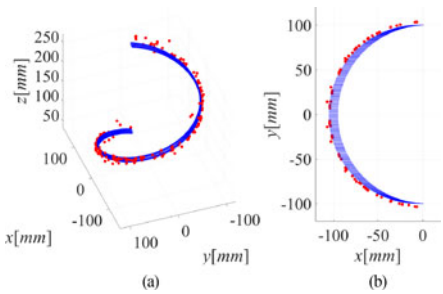

Fig. 5. Reconstructed points (red circle) by the proposed RPM. (a) 3-D view. (b) Sliced view (100 mm $\leq z \leq$ 200 mm).

source current forms a Gaussian-modulated pulse with a center frequency of 3.0 GHz, and an effective bandwidth of 2.0 GHz and is linearly excited along the z-axis. The electric field for the z-coordinate component is recorded at each receiver, which is located at the same position as the transmitter. The outer dielectric medium is assumed to be homogeneous and lossy concrete material, with a relative permittivity of 7.0 and conductivity of 0.001 S/m. A spiral-shaped air cavity is buried in the concrete object with a 10 mm cross-sectional diameter. The observation setup is shown in Fig. 1. The set of transmitting and receiving antennas is scanned along a cylindrical orbit having a radius of 400 mm and height of 300 mm, where the observation points are equally sampled with 11 points along the azimuthal direction for $0 \leq \theta \leq 2\pi$ and with 7 points along the z-axis are equally sampled for $0 \leq z \leq 300$ mm. Fig. 3 shows the cross-sectional images reconstructed by the DAS-based method on $z = 150$ mm and $z = 200$ mm planes. In each cross-sectional image, there are many undesired responses caused by the grating lobe effect, and the actual cavity shape is hardly identifiable from this image. Figs. 4 and 5 show the reconstruction results of the original and the proposed RPM-based method, respectively. Note that the sliced view as in the right-hand sides of Figs. 4 and 5 denotes the projected view for the 3-D volume with thickness as 100 mm $\leq z \leq$ 200 mm. Here, the original RPM method uses

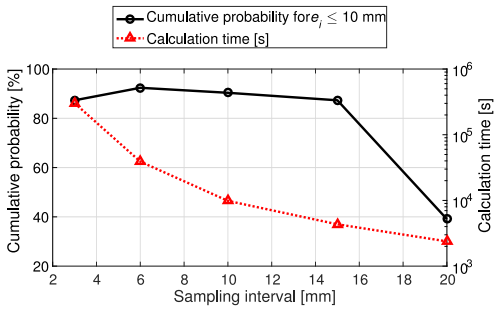

Fig. 6. Cumulative probability for $e_i \leq 10$ mm and calculation time of the original RPM vs. sampling interval of outer boundary.

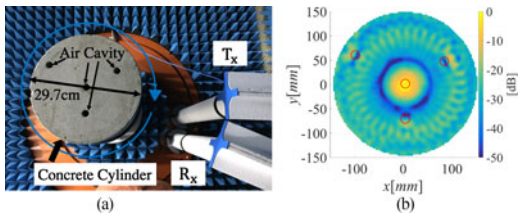

Fig. 7. (a) Experimental setup. (b) Cross-sectional image obtained by the DAS-based method on $z = 93$ mm plane.

a 3 mm sampling interval for the outer boundary, and the parameters are set as $\sigma_r = 10$ mm, $\sigma_{XY} = \sigma_Z = 50$ mm, and $\sigma_R = 30$ mm. The quasi-Newton method is applied for the optimization in (3). These figures indicate that the RPM-based methods accurately reconstruct the spiral shape of the air cavity. For a quantitative evaluation, an estimation error of the ith estimated point is defined as

$$e_i = \min_{\boldsymbol{r}_{\rm true}} \|\boldsymbol{r}_{\rm true} - \boldsymbol{r}_i\| \tag{4}$$

where $\boldsymbol{r}_{\rm true}$ is the location of the true target point. Each cumulative probability for satisfying $e_i \leq 10$ mm is 87% for the original RPM method and 92% for the proposed method. Furthermore, the calculation time with Intel Xeon CPU E5-2620 2.4 GHz processor and 128 GB RAM is 3.0×10^5 s for the original RPM-based method and 7.6×10^2 s for the proposed method. Thus, the proposed method achieves about 394 times acceleration from the original method. To evaluate the accuracy of the original RPM-based method for various sampling intervals, the cumulative probability for for satisfying $e_i \leq 10$ mm and the required calculation time are plotted against the sampling intervals of the outer boundary, as shown in Fig. 6. The results indicate that even in most sparsely sampled case, the original method requires about 2.3×10^3 s and suffers from considerable inaccuracy with 39% cumulative probability for satisfying $e_i \leq 10$ mm. These results demonstrate that our proposed method is superior to the original method irrespective of the sampling interval. Note that, if the outer boundary has a sharp edge like square pillar, it would cause some errors due to not considering the edge diffraction effect in these methods. In this case, there would be also missing area due to a lack of reflection echo from a part of inner object; however, this kind problem could be improved by the multistatic observation model as in [8].

B. Experimental Test

This section describes experimental validations for each method performed. Fig. 7(a) shows the experimental setup, where the two vertical dipole antennas are fixed as the

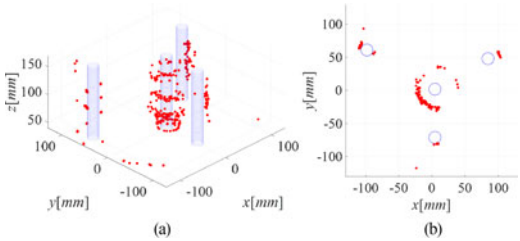

Fig. 8. Reconstructed points (red circles) by the original RPM. (a) 3-D view. (b) sliced view (70 mm $\leq z \leq$ 110 mm).

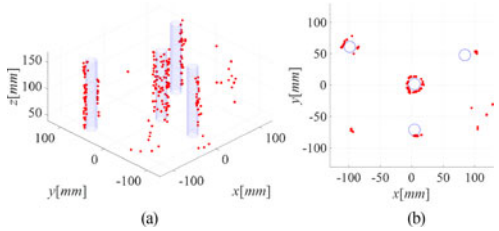

Fig. 9. Reconstructed points (red circles) by the proposed RPM. (a) 3-D view. (b) sliced view (70 mm $\leq z \leq$ 110 mm).

transmitting and receiving antennas with a separation of 150 mm. A cylindrical concrete object with a height of 250 mm and a diameter of 297 mm is placed at the center of an azimuth rotating table. Here, the relative permittivity of the concrete material is calculated as 9.6 using the free-space permittivity measurement method. Four cylindrical air cavities (diameter: 18 mm; height: 250 mm) are buried in the concrete material. To achieve the cylindrical scanning model as used in the numerical test, the concrete object is rotated by 10° intervals. This object is also moved along the z-axis for 43 mm $\leq z \leq$ 168 mm with an interval of 25 mm using a mechanical lifter. The reflection data are obtained using a vector network analyzer, where a frequency sweep from 1.0 to 2.6 GHz occurs at an interval of 10 MHz. Fig. 7(b) shows the the cross-sectional DAS image on $z = 93$ mm plane. Also, Figs. 8 and 9 show the reconstruction results by the original and the proposed RPM-based method, respectively. Here, the original RPM method uses 3 mm sampling interval for outer boundary, and the parameters of the RPM method are set as $\sigma_r = 2$ mm, $\sigma_{XY} = 90$ mm, $\sigma_Z = 30$ mm, and $\sigma_R = 25$ mm. Each cumulative probability for satisfying $e_i \leq 10$ mm is 61% for the original RPM method and 88% for the proposed method. The calculation time is 7.1×10^5 s for the original RPM-based method, and is 6.6×10^4 s for the proposed method with the same processor and RAM in numerical test, and the proposed method achieves approximately ten times acceleration from the original method. Note that the artifact point appeared in the sliced view in Fig. 9, where the corresponding target point by the original RPM also generates the artifact around $z = 50$ mm, which is not included in the sliced view in Fig. 8. This artifact is caused by the remaining components from the surface clutter suppression.

VI. Conclusion

This letter introduced an acceleration of RPM-based imaging method. FDTD-based numerical test and experimental test demonstrate that the proposed method accurately reconstructs targert boundary compared with DAS-based method, and enhances the imaging speed with maintaining the accuracy obtained by the original RPM-based method. The imaging accuracy of this method depends on the range resolution, especially for separating the reflection echoes from outer boundary, and embedded object, which could be partially solved by the super resolution range extraction filter [9]. In addition, in the case of heterogeneous background media, the imaging accuracy would also degrade, but [4] has revealed that there is no serious sensitivity for such heterogeneity. In the case that a target boundary has roughness within a wavelength, the RPM and other imaging methods suffer from inaccuracy for boundary reconstruction because the received signal is distorted from the reference one due to scattering effect. Reference [9] also denotes one solution for the above problem, introducing the fractional derivative-based waveform matching. Furthermore, the RPM method has a notable feature for associating range point and target point with one-to-one correspondence, which enables us more multifunctional imaging, such as the incorporation with Doppler component [10], or fully polarimetric data [11] or permittivity [12], and has a great potential to enhance the recognition performance. We also consider that it is promising to incorporate DAS-based algorithm with RPM method to enhance the azimuth resolution, or to accelerate the F-k migration process [1], with complex-valued-based postprocessing as in [13].

References

[1] M. Fallahpour, J. T. Case, M. Ghasr, and R. Zoughi, "Piecewise and wiener filter-based sar techniques for monostatic microwave imaging of layered structures," *IEEE Trans. Antennas Propag.*, vol. 62, no. 1, pp. 1–13, Jan. 2014.

[2] M. Maffongelli *et al.*, "Reconstruction of metallic inclusions inside dielectric targets by means of a microwave tomographic system," *IEEE Microw. Wireless Compon. Lett.*, vol. 22, no. 7, pp. 378–380, Jul. 2012.

[3] S. Kidera, T. Sakamoto, and T. Sato, "Accurate UWB radar 3-D imaging algorithm for complex boundary without range point connections," *IEEE Trans. Geosci. Remote Sens.*, vol. 48, no. 4, pp. 1993–2004, Apr. 2010.

[4] K. Akune, S. Kidera, and T. Kirimoto, "Accurate and nonparametric imaging algorithm for targets buried in dielectric medium for UWB radars," *IEICE Trans. Electron.*, vol. E95-C, no. 8, pp. 1389–1398, Aug. 2012.

[5] S. Kidera and T. Kirimoto, "Efficient three-dimensional imaging method based on enhanced range point migration for UWB radars," *IEEE Geosci. Remote Sens. Lett.*, vol. 10, no. 5, pp. 1104–1108, Sep. 2013.

[6] S. Kidera, T. Sakamoto, and T. Sato, "A robust and fast imaging algorithm with an envelope of circles for UWB pulse radars," *IEICE Trans. Commun.* vol. E90-B, no. 7, pp. 1801–1809, Jul. 2007.

[7] S. Takahashi and S. Kidera, "Acceleration of RPM-based microwave imaging for non-destructive testing," in *Proc. IEEE Int. Symp. Antennas Propag.*, Oct. 2017, pp. 1–2.

[8] Y. Niwa, S. Kidera, and T. Kirimoto, "Image expansion approach for target buried in dielectric medium with extended RPM to multi-static UWB radar," *IEICE Trans. Electron.*, vol. E96-C, no. 1, pp. 119-123, Jan. 2013.

[9] S. Kidera, T. Sakamoto, and T. Sato, "Super-resolution UWB radar imaging algorithm based on extended capon with reference signal optimization," *IEEE Trans. Antennas Propag.*, vol. 59, no. 5, pp. 1606–1615, May 2011.

[10] Y. Sasaki, F. Shang, S. Kidera, T. Kirimoto, K. Saho, and T. Sato, "Three-dimensional imaging method incorporating range points migration and doppler velocity estimation for UWB millimeter-wave radar," *IEEE Geosci. Remote Sens. Lett.*, vol. 14, no. 1, pp. 122–126, Jan. 2017.

[11] A. Yamaryo, T. Takatori, S. Kidera, and T. Kirimoto, "Range points migration based image expansion method exploiting fully polarimetric data for UWB short-range radar," *IEEE Trans. Geosci. Remote Sens.*, to be published, doi: 10.1109/TGRS.2017.2776274.

[12] T. Takatori and S. Kidera, "Permittivity imaging method by incorporating range points migration and ellipsometry for UWB short range radar," in *Proc. Prog. Electromagn. Res. Symp.*, Nov. 2017, pp. 1–4.

[13] Y. Alvarez, B. Gonzalez-Valdes, J. A. Martinez, F. Las-Heras, and C. M. Rappaport, "An improved SAR based technique for accurate profile reconstruction." *IEEE Trans. Antennas Propag.*, vol. 61, no. 3, pp. 1490–1495, Mar. 2013.